Nanoscale

CORRECTION

View Article Online
View Journal | View Issue

Cite this: *Nanoscale*, 2018, **10**, 14771

Correction: Lithographically fabricated gold nanowire waveguides for plasmonic routers and logic gates

Long Gao,[a,b] Li Chen,[a] Hong Wei*[a] and Hongxing Xu[c]

DOI: 10.1039/c8nr90158a

rsc.li/nanoscale

Correction for 'Lithographically fabricated gold nanowire waveguides for plasmonic routers and logic gates' by Long Gao *et al.*, *Nanoscale*, 2018, **10**, 11923–11929.

The authors have noticed an error in Fig. 6 in the published paper, in which Fig. 6b and Fig. 5c are identical due to an error that occurred in the production stage of the paper. The correct version of Fig. 6 is shown below, and the caption of the figure remains the same. This error does not affect the conclusions of the paper.

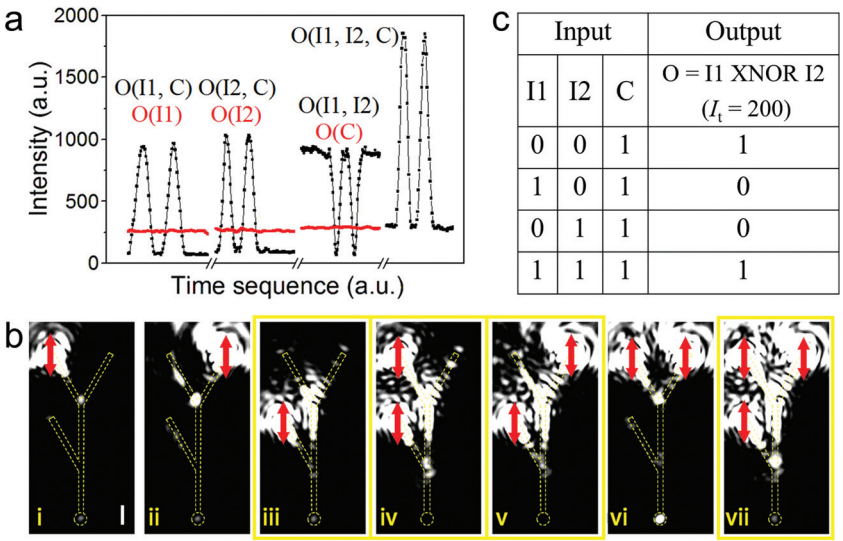

c

Input			Output
I1	I2	C	O = I1 XNOR I2 (I_t = 200)
0	0	1	1
1	0	1	0
0	1	1	0
1	1	1	1

Fig. 6 Interference of SPs in a gold NW network with three inputs for the XNOR gate. (a) Output intensity for single inputs (red) and multiple inputs (black) with the phase difference changing over time. The plateaus on the sides of the oscillating curves correspond to the minimum or maximum output intensity for fixed phases. (b) (i–iii) Scattering images for single inputs. (iv–vii) Scattering images for two or three inputs. The scattering images outlined by yellow boxes show the working states corresponding to the XNOR operations. The red arrows indicate the polarization of incident light. The scale bar is 1 μm. (c) Inputs and outputs of the XNOR logic gate.

The Royal Society of Chemistry apologises for this error and any consequent inconvenience to authors and readers.

[a]*Beijing National Laboratory for Condensed Matter Physics, Institute of Physics, Chinese Academy of Sciences, Beijing 100190, China. E-mail: weihong@iphy.ac.cn*
[b]*School of Physical Sciences, University of Chinese Academy of Sciences, Beijing 100049, China*
[c]*School of Physics and Technology, and Institute for Advanced Studies, Wuhan University, Wuhan 430072, China*

Nanoscale

PAPER

View Article Online
View Journal | View Issue

Cite this: *Nanoscale*, 2018, **10**, 11923

Lithographically fabricated gold nanowire waveguides for plasmonic routers and logic gates†

Long Gao,[a,b] Li Chen,[a] Hong Wei *[a] and Hongxing Xu [c]

Received 3rd March 2018,
Accepted 21st May 2018

DOI: 10.1039/c8nr01827h

rsc.li/nanoscale

Fabricating plasmonic nanowire waveguides and circuits by lithographic fabrication methods is highly desired for nanophotonic circuitry applications. Here we report an approach for fabricating metal nanowire networks by using electron beam lithography and metal film deposition techniques. The gold nanowire structures are fabricated on quartz substrates without using any adhesion layer but coated with a thin layer of Al_2O_3 film for immobilization. The thermal annealing during the Al_2O_3 deposition process decreases the surface plasmon loss. In a Y-shaped gold nanowire network, the surface plasmons can be routed to different branches by controlling the polarization of the excitation light, and the routing behavior is dependent on the length of the main nanowire. Simulated electric field distributions show that the zigzag distribution of the electric field in the nanowire network determines the surface plasmon routing. By using two laser beams to excite surface plasmons in a Y-shaped nanowire network, the output intensity can be modulated by the interference of surface plasmons, which can be used to design Boolean logic gates. We experimentally demonstrate that AND, OR, XOR and NOT gates can be realized in three-terminal nanowire networks, and NAND, NOR and XNOR gates can be realized in four-terminal nanowire networks. This work takes a step toward the fabrication of on-chip integrated plasmonic circuits.

Introduction

As semiconductor-based electronic devices are approaching their physical limit, photonic devices possessing good performance in both speed and heat load can be ideal successors.[1] Surface plasmons (SPs) attract much attention because circuits based on SPs can guide light at the nanoscale and overcome the diffraction limit that has constrained the size of photonic devices.[2] To build plasmonic circuits, many fundamental components, such as plasmonic waveguides, routers, modulators, amplifiers, switches, sources, detectors, logic gates, *etc.*, need to be explored.[3–17] Plasmonic waveguide is a basic and indispensable component that can support light transmission with nanoscale field confinement which is critical for the miniaturization of photonic circuits. Metal nanowires (NWs) are a typical kind of plasmonic waveguide, supporting the long range propagation of various SP modes.[4,10,18–22] Metal NWs behave like Fabry–Pérot resonators with the propagating SPs reflected at the ends of the NWs.[18,23,24] The SPs on metal NWs can couple with quantum emitters,[25–32] and semiconductor NWs,[33,34] which can be utilized to design active plasmonic devices.

The metal NWs used for guiding the propagating SPs are usually chemically synthesized with monocrystalline structures and low propagation loss.[4] By assembling chemically-synthesized silver NWs into networks, plasmonic routers and logic gates were demonstrated.[5,6,13,14] However, chemically synthesized NWs have low consistency in dimensions, and the fabrication of NW networks requires assembling techniques like micromanipulation which has low yield and accuracy. These shortcomings limit the applications of chemically synthesized metal NWs in practical use. With the development of nanofabrication techniques in recent years, lithographic fabrication method and focused ion beam milling fabrication method can provide high yield and controllability in the fabrication of metal NWs.[24,35–38] Of these two approaches, lithographic fabrication can provide even higher fabrication efficiency than focused ion beam milling. Standard electron beam lithography (EBL) uses polymethyl methacrylate (PMMA) on a target substrate as a resist. After exposure and development, a metal film is evaporated on the substrate followed by a lift-off process.[39] Previous studies show that the metal NWs fabricated by the lithographic method are polycrystalline and suffer large SP propagation loss.[24] Due to the low SP propagation efficiency, there has been no controllable routing or

[a]*Beijing National Laboratory for Condensed Matter Physics, Institute of Physics, Chinese Academy of Sciences, Beijing 100190, China. E-mail: weihong@iphy.ac.cn*
[b]*School of Physical Sciences, University of Chinese Academy of Sciences, Beijing 100049, China*
[c]*School of Physics and Technology, and Institute for Advanced Studies, Wuhan University, Wuhan 430072, China*

†Electronic supplementary information (ESI) available. See DOI: 10.1039/c8nr01827h

logic functions demonstrated in metal NW networks fabricated by the lithographic method.

Here in this paper we demonstrate an approach for the lithographic fabrication of gold NW networks and use them as plasmonic routers and logic gates. By removing the usually used adhesion layer between gold and the substrates and coating the NWs with Al_2O_3 by atomic layer deposition, the propagation loss of SPs on the gold NWs is considerably decreased with the help of thermal annealing during the Al_2O_3 deposition process. A Y-shaped NW network can serve as a controllable router by engineering the length of the main wire and controlling the polarization of the incident light. The control of SP interference in the NW networks is realized by adjusting the phase delay of SPs excited from different input ends. Based on SP interference, the functions of seven fundamental logic gates are experimentally demonstrated in gold NW networks with three or four terminals. This work provides an effective approach for fabricating metal NWs and NW networks for integrated plasmonic circuit applications.

Experimental and theoretical methods

Sample fabrication and optical measurements

The gold NWs are fabricated by the lithographic method based on EBL and vacuum deposition of a metal (Fig. 1a). PMMA resist is spin-coated on quartz substrates and a thin chromium layer of 4 nm thickness is evaporated on top of the resist to serve as a conducting layer. The nanostructure patterns are written with a standard EBL exposure process and then the chromium layer is removed by a wet etching process. After development and fixing, the substrate is transferred to a vacuum chamber for depositing a gold film of 150 nm thickness by thermal evaporation (chamber pressure at 5×10^{-4} Pa). After the gold deposition, the sample is treated with a careful lift-off process by immersing it in acetone for 30 min at 65 °C. After this lift-off process, more than 90% of the gold nanostructures without any adhesion layer can remain on the substrate over a large area. Then an Al_2O_3 coating layer is deposited on the sample surface by atomic layer deposition (the temperature of the chamber is 200 °C and the deposition process lasts 30 min). Fig. 1b shows the scanning electron microscopy (SEM) images for a typical straight NW and a Y-shaped NW network with 150 nm width.

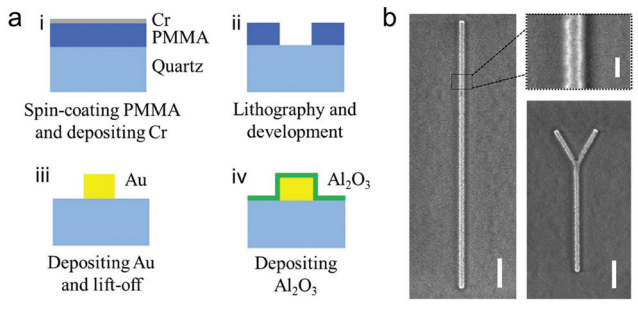

Fig. 1 (a) Lithographic fabrication procedures of the gold NWs. (b) SEM images of a straight gold NW and a Y-shaped NW. The scale bar is 200 nm for the image at the upper right corner and 1 μm for the remaining two images.

The optical measurements are performed on an upright optical microscope with a piezo stage for positioning the samples. SPs are generated with a 785 nm laser by focusing the laser light at the end of the NW under an objective (×100, NA = 1.49 in oil, or ×100, NA = 0.9 in air). The SPs propagate to the distal end of the NW where they are scattered into photons that are collected by using the same objective and detected by using a CCD camera. The power, polarization and phase of the incident light can be adjusted by attenuation plates, half-wave plates and Soleil–Babinet compensators, respectively.

Numerical simulations

The waveguide modes and near field distributions on gold NWs are calculated using a finite element method based commercial software (COMSOL Multiphysics). The mode profiles in the cross section of the gold NW and the effective refractive indices of the SP modes are obtained using the mode solver. The interference between multiple SP modes leads to specific near field distributions, which are calculated using the "Wave Optics-Frequency Domain" module in three-dimensional space. A Gaussian beam of 785 nm wavelength with 1 μm waist diameter is inserted perpendicular to the NW axis at one of the NW ends to excite the propagating SPs. The permittivity for gold ($\varepsilon_{Au} = -22.85 + 1.42i$) is taken from Johnson and Christy.[40] The refractive index of Al_2O_3 ($n = 1.76$) is taken from Malitson and Dodge.[41] The NWs are placed in a surrounding medium with refractive index $n = 1.518$.

Results and discussion

Characterization of SP propagation on gold NWs

When the laser is focused at the end of the gold NW with the polarization parallel to the NW, SPs are launched and propagate along it. Scattering light can be detected at the distal end of the NW due to the SPs converting to photons therein (Fig. 2a). In the standard lithographic fabrication of gold nanostructures, an adhesion layer consisting of a metal like chromium or titanium is usually used to increase the adhesion of the gold to the substrate. The adhesive metal layer introduces additional loss to the SPs.[36,42–44] Our results for the gold NWs with and without the chromium layer show that the chromium strongly damps the propagating SPs (see Fig. S1 in the ESI†). Therefore, we omit the adhesion layer and deposit gold directly on the quartz substrates to obtain the gold NW waveguides. To immobilize the NWs onto the substrate, we deposit an Al_2O_3 film onto the surface of the gold NWs. The coating layer also protects the gold NWs from exposure to the surrounding environment.

Fig. 2b shows the intensity of scattering light at the output ends of the gold NWs in different surrounding media for NWs of different lengths on the same sample. As can be seen, after

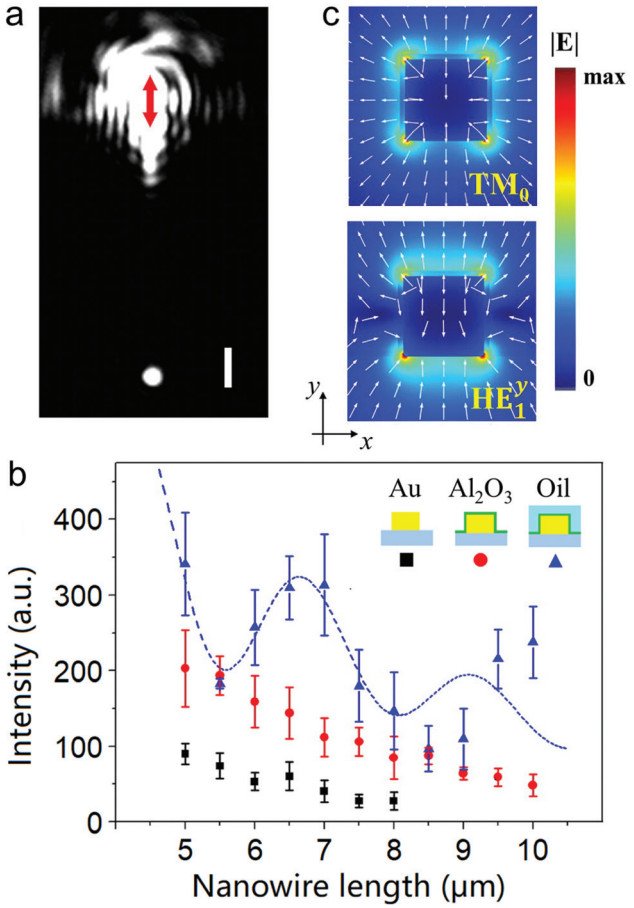

Fig. 2 (a) Scattering image of a gold NW with a 785 nm laser beam focused at one end. The scale bar is 1 μm. The incident polarization is shown by the arrow. (b) Intensity of scattering light from the output ends of gold NWs as a function of NW length for the bare gold NWs (black squares), for the gold NWs with 10 nm thick Al_2O_3 deposited (red circles), and for the 10 nm Al_2O_3 coated gold NWs immersed in index-matching oil (blue triangles). The inset shows the schematic illustration of the samples. Each point represents the mean value of the output intensity from seven different NWs with the same geometry. The error bars show the standard deviation. The blue dashed line is the fitting result using the calculated effective refractive indices of two SP modes. (c) Electric field distributions of two modes (TM_0 and HE_1^y) of SPs on a gold NW in a homogeneous medium with a refractive index of 1.518. The width and height of the NW are both 150 nm. The NW is covered by an Al_2O_3 layer of 10 nm thickness to mimic the experimental sample.

the deposition of the Al_2O_3 coating layer, the light intensity at the output ends of the NWs is obviously increased, which indicates the decrease of SP loss (comparing the red circles and black squares in Fig. 2b). It is determined that the loss decrease results from the structural modifications of the NWs induced by the thermal annealing in the process of depositing Al_2O_3 (see Fig. S2 and S3 in the ESI†).[45,46] Then the sample is illuminated through an oil immersion objective. The intensities of the collected signals at the ends of the NWs are further increased (the blue triangles in Fig. 2b), as the high numerical aperture of the objective provides larger excitation and collection efficiency and the homogeneous surrounding medium prevents the leakage radiation of SPs.[47,48] A strong oscillation of the intensity related to the NW length shows up when the NWs are in the homogeneous surrounding medium, which is attributed to the superposition of two different SP modes excited in the NWs.[6,21] Fig. 2c shows the electric field distributions of the two modes (TM_0 and HE_1^y), which can be excited by light polarized parallel to the NW. The fitted curve in Fig. 2b is obtained by fitting the experimental data with the simulated wave vectors of the two modes (see section 2 in the ESI†). These results show that polycrystalline NWs fabricated by the lithographic method and treated with the deposition of an Al_2O_3 coating layer can be used as plasmonic waveguides with good performance, which makes them qualify for applications in plasmonic circuits.

Controllable routing of SPs in Y-shaped NW networks

Fig. 3a, d and f show the optical images of three fabricated Y-shaped NW networks with different lengths of the vertical main wire. The scattering images in Fig. 3b and c show that the emission intensity at the two output ends of the Y-shaped branch structure is dependent on the polarization of the incident light. For the polarization angle $\theta = 60°$ and $\theta = -60°$ (θ represents the angle between the incident polarization and the main wire, as marked in Fig. 3a), the SPs will mostly propagate to the left branch and the right branch, respectively, when the main wire length is 3.4 μm. The SP routing behavior is dependent on the length of the main wire. Fig. 3e and g show that, under the excitation of $\theta = 60°$, the SPs split and propagate to the two branches equally when the main wire length is

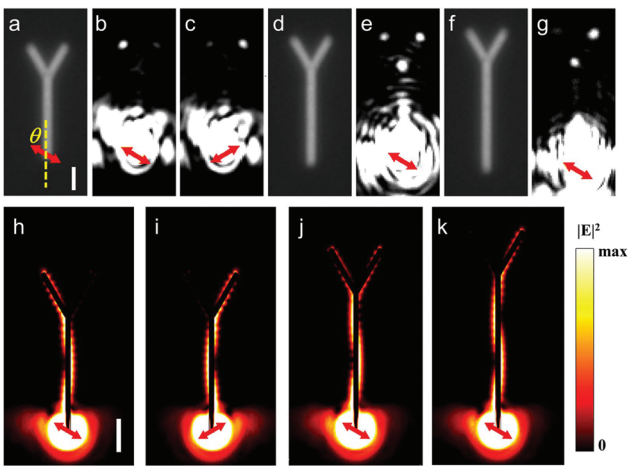

Fig. 3 (a, d, f) Optical images of Y-shaped gold NW networks. The length of the main wires is (a) 3.4 μm, (d) 4 μm, and (f) 4.6 μm. The definition of polarization angle θ is marked in (a). (b, c, e, g) Scattering images when the Y-shaped NW networks in (a, d, f) are under linearly polarized illumination. The polarization of the incident light is marked by the arrows. (h–k) Simulation results for the distribution of the electric field intensity in Y-shaped NW networks. The distributions are on the horizontal plane across the center of the NWs. The polarization of the excitation light is marked by the arrows. The length of the main wires is (h, i) 3.4 μm, (j) 4 μm, and (k) 4.6 μm. The scale bars in (a) and (h) are 1 μm, and also apply to (b–g) and (i–k), respectively.

4 μm, while the SPs propagate mostly to the right branch when the main wire length is 4.6 μm.

The SP routing behavior is determined by the near field distributions at the junction of the Y-shaped branch structure, resulting from the superposition of multiple SP modes. In addition to the two modes in Fig. 2c, the NW supports the HE_1^x mode that can be excited by light polarized perpendicular to the NW. When the main wire end is under incident light with appropriate polarization, these three lowest order modes (TM_0, HE_1^x and HE_1^y) can be excited and propagate along the NW.[21] When the incident polarization is parallel or perpendicular to the main wire ($\theta = 0°$ or 90°), the electric field is symmetrically distributed on the two sides of the junction in the Y-shaped NW network; thus the SPs will propagate equally to the two branches. For $0° < \theta < 90°$, the electric field distribution on the NW is in a zigzag shape. Therefore, the electric field intensity on the two sides of the branch junction can be different, which will influence the routing behavior of the propagating SPs. Fig. 3h–k show the simulation results of the electric field distributions for three structures corresponding to the experimental ones. For the structure with the main wire of a length of 3.4 μm, the asymmetric distribution of the electric field at the junction determines that the SPs will propagate to the side with strong intensity, resulting in the SP routing (Fig. 3h and i). When the length of the main wire is increased to 4 μm, the electric field intensity on the two sides of the junction is similar, so the SPs propagate to the two branches, resulting in similar output intensities on them (Fig. 3j). For the NW structure with the main wire length of 4.6 μm, the field distribution at the junction becomes asymmetric again, but the strong field is on the opposite side of the junction for the same incident polarization compared to the structure with the main wire length of 3.4 μm. Therefore, the SPs will propagate to a different branch (comparing Fig. 3k and h). All simulation results are in good agreement with the experimental results. The SP routing behavior can thus be precisely controlled by the incident polarization and the geometry of the structure. The maximum switching ratio is reached when the incident polarization angle is ±60° because of the different intensities of the SP modes (see section 3 in the ESI†).

Boolean logic in NW networks

Two SP waves can be launched in the Y-shaped NW structure by focusing two laser beams on the two ends I1 and I2 (Fig. 4a). The two SP waves interfere on the main wire, which modulates the output light intensity at the distal end O. The phase difference of the incident light at I1 and I2 terminals can be controlled by a Soleil–Babinet compensator in the light path. When only one laser beam is focused on either the I1 or I2 input end, the output intensity is similar and irrelevant to the incident phase (Fig. 4b, black and red crosses). When the two laser beams are both turned on and the phase of the I2 input is tuned, the output intensity will oscillate between the maximum and minimum values (Fig. 4b, blue crosses) due to interference. As can be seen that the SPs from the two inputs interfere strongly and the interference visibility $V = (I_{max} - I_{min})/(I_{max} + I_{max})$ is over 0.83. Fig. 4c shows the scattering images for either the I1 or I2 input (Fig. 4ci, ii), and for both the I1 and I2 inputs with constructive (Fig. 4ciii) and destructive (Fig. 4civ) interference.

By assigning the input and output signals to "1" or "0", this NW network can serve as three-terminal Boolean logic gates. The output is "1" for intensity larger than the threshold intensity I_t, and is "0" for intensity lower than I_t. Fig. 4d shows the truth table of four logic gates. When I_t is 200, the NW network can serve as an AND gate for constructive interference. When I_t is set to 100, the NW network can execute the logic operations of OR for constructive interference. With an additional phase difference π leading to destructive interference, the NW network can work as an XOR gate. If the I2 input is defined as a control signal, the output state will be opposite to the I1 input; thus the NW network executes the NOT logic operations.

NAND and NOR gates, the so-called universal logic gates, can be realized in the NW network with three input ends and one output end (Fig. 5a), where an additional control input C is added into the Y-shaped NW network. The incident power for three inputs is adjusted by attenuators so that the output intensity O(I1) and O(I2) are both about 300 while O(C) is about 1000 (red lines in Fig. 5b). The corresponding scattering images are shown in Fig. 5ci, ii, and iii, respectively. At first, the I1 and C inputs are both turned on. The interference of the two launched SP waves results in the oscillation of output intensity O(I1, C) by tuning the phase of input C. The destructive interference leads to the minimum of O(I1, C) with the intensity close to O(I1) [O(I1, C) in Fig. 5b and panel iv in Fig. 5c]. Then the I1 input is blocked and the I2 input is turned on. Tuning the phase of the I2 input can lead to the minimum of O(I2, C) for destructive interference [O(I2, C) in Fig. 5b and panel v in Fig. 5c]. Then the C input is blocked and the I1 input is turned on again. It is found that the intensity of O(I1, I2) is close to O(C) and is the maximum value for the interference of the I1 and I2 inputs [O(I1, I2) in Fig. 5b and panel vi in Fig. 5c]. For the phase corresponding to the maximum O(I1, I2), the output intensity for all three inputs turned on O(I1, I2, C) is significantly lower than O(I1) or O(I2) [O(I1, I2, C) in Fig. 5b and panel vii in Fig. 5c], which is the minimum value of O(I1, I2, C) as confirmed by the oscillating O(I1, I2, C) intensity for varied phases of input C. Now the phase of the C and I2 inputs are fixed, which corresponds to the constructive interference of I1 with I2 and destructive interference of both I1 and I2 with C. When I_t is defined as 200, which is above O(I1, I2, C) and below O(I1) and O(I2), the outputs correspond to the NAND logic operations. When I_t is defined as 500, which is above O(I1) and O(I2) and below O(C), the outputs correspond to the NOR logic operations (Fig. 5d). In addition to the realization method discussed above, NAND and NOR gates can also be realized by cascading the AND and OR gates with the NOT gate, respectively (section 4 in the ESI†).

If the intensity of O(C) is the same as the intensity of O(I1) and O(I2), the XNOR gate can be realized in the same NW network structure. A similar measurement is carried out and the output intensity changes for the varied phases are shown

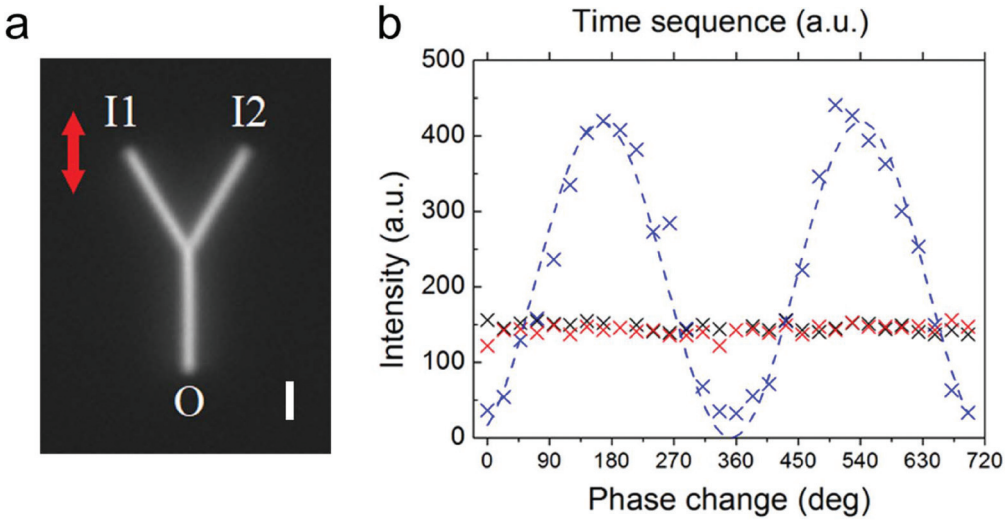

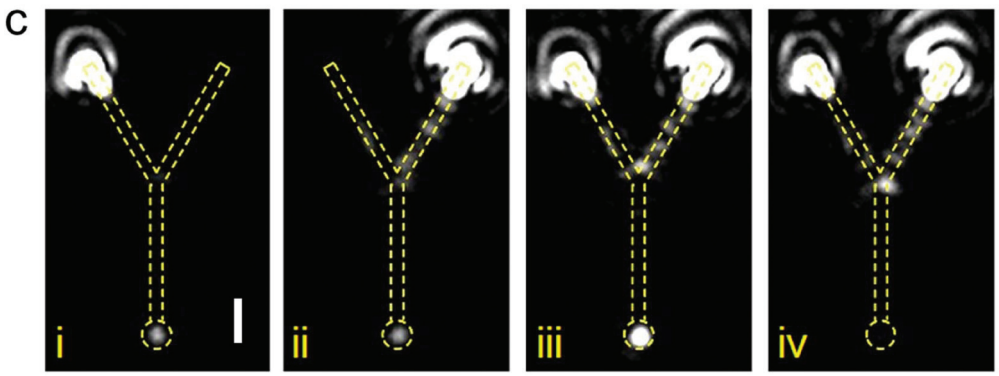

d

Input		Output			
I1	I2	O = I1 AND I2 (I_t = 200)	O = I1 OR I2 (I_t = 100)	O = I1 XOR I2 (I_t = 100)	O = NOT I1 (I2 as control, I_t = 100)
0	0	0	0	0	
1	0	0	1	1	
0	1	0	1	1	1
1	1	1	1	0	0

Fig. 4 Interference of SPs in a Y-shaped gold NW structure with two inputs. (a) Optical image of a Y-shaped NW network. The scale bar is 1 μm. The length of each NW is 3 μm and the width is 150 nm. The arrow indicates the polarization of the incident light. (b) Blue crosses: output intensity as a function of phase difference between inputs I1 and I2. Black and red crosses: output intensity *versus* time when either I1 (black) or I2 (red) is turned on. The blue dashed line is a fit curve of sine square. (c) (i, ii) Scattering images when either I1 or I2 is turned on. (iii, iv) Scattering images for constructive and destructive interference of SPs excited from I1 and I2. The scale bar is 1 μm. (d) Inputs and outputs of four Boolean logic gates (AND, OR, XOR, and NOT) realized in the three-terminal NW network.

in Fig. 6a. The intensities of O(I1), O(I2) and O(C) are shown in Fig. 6a as red lines (about 270) and the corresponding scattering images are shown in Fig. 6bi–iii. The I1 and C inputs are tuned to be out of phase by π to reach a minimum output intensity [O(I1, C) in Fig. 6a and panel iv in Fig. 6b]. Then the phase of the C input is fixed and I2 is tuned to be out of phase by π with the C input [O(I2, C) in Fig. 6a and panel v in Fig. 6b]. This means that the I1 and I2 inputs are in phase and the interference results in the maximum output intensity [O(I1, I2) in Fig. 6a and panel vi in Fig. 6b]. When all three inputs are turned on, it is found that the intensity of O(I1, I2, C) is very close to the intensity of O(I1), O(I2), and O(C) (Fig. 6bvii). Tuning the phase of the C input proves that this intensity of O(I1, I2, C) is the minimum value for the inter-

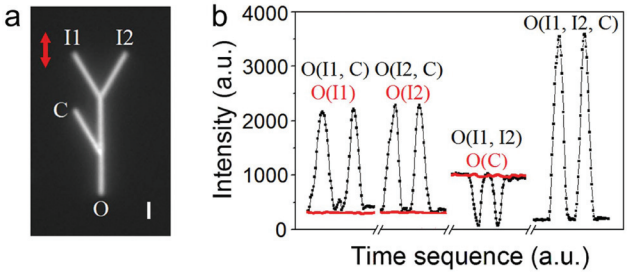

d

Input			Output	
I1	I2	C	O = I1 NAND I2 (I_t = 200)	O = I1 NOR I2 (I_t = 500)
0	0	1	1	1
1	0	1	1	0
0	1	1	1	0
1	1	1	0	0

Fig. 5 Interference of SPs in a gold NW network with three inputs for NAND and NOR gates. (a) Optical image of the NW network. The scale bar is 1 μm. (b) Output intensity for single inputs (red) and multiple inputs (black) with the phase difference changing over time. The plateaus on the sides of the oscillating curves correspond to the minimum or maximum output intensity for fixed phases. (c) (i–iii) Scattering images for single inputs. (iv–vii) Scattering images for two or three inputs. The scattering images outlined by yellow boxes show the working states corresponding to the NAND and NOR operations. The scale bar is 1 μm. (d) Inputs and outputs of NAND and NOR logic gates. The red arrows indicate the polarization of incident light.

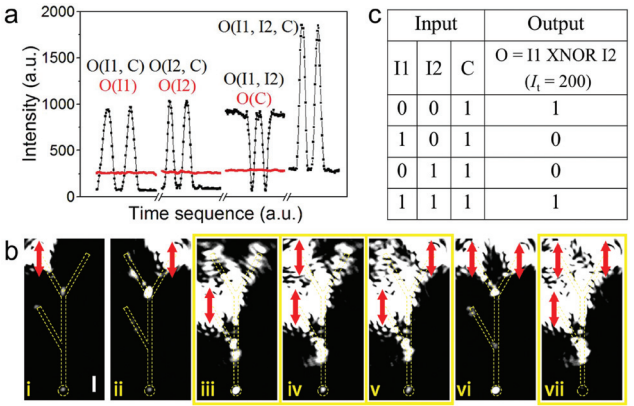

c

Input			Output
I1	I2	C	O = I1 XNOR I2 (I_t = 200)
0	0	1	1
1	0	1	0
0	1	1	0
1	1	1	1

Fig. 6 Interference of SPs in a gold NW network with three inputs for the XNOR gate. (a) Output intensity for single inputs (red) and multiple inputs (black) with the phase difference changing over time. The plateaus on the sides of the oscillating curves correspond to the minimum or maximum output intensity for fixed phases. (b) (i–iii) Scattering images for single inputs. (iv–vii) Scattering images for two or three inputs. The scattering images outlined by yellow boxes show the working states corresponding to the XNOR operations. The red arrows indicate the polarization of incident light. The scale bar is 1 μm. (c) Inputs and outputs of the XNOR logic gate.

ference with different phases of input C [O(I1, I2, C) in Fig. 6a]. If the threshold I_t is defined as 200, which is below O(I1), O(I2), and O(C) and above the minimum of O(I1, C) and O(I2, C), the output states correspond to the XNOR operations (Fig. 6c).

Conclusion

We demonstrate an approach for fabricating gold NW networks by EBL and metal film deposition techniques, and realize the plasmonic routers and Boolean logic gates in the fabricated structures. The Al_2O_3 coating layer can immobilize the gold NWs without an adhesion layer onto the substrate, and the thermal annealing during the Al_2O_3 deposition process decreases the SP propagation loss. Polarization controlled plasmon routing function is realized in Y-shaped gold NW networks, which is strongly dependent on the length of the main wire. The output intensity in the NW network can be modulated when exciting the SPs by multiple laser beams due to the interference of SPs. AND, OR, XOR and NOT gates are realized in three-terminal NW networks and NAND, NOR and XNOR gates are realized in four-terminal NW networks. The lithographic fabrication method reported in this work can be easily applied to other metals and various substrates, facilitating the on-chip integration of plasmonic devices for optical information guiding and processing.

Conflicts of interest

There are no conflicts to declare.

Acknowledgements

This work was supported by the Ministry of Science and Technology of China (Grant No. 2015CB932400), the National Natural Science Foundation of China (Grant No. 11422436, 11674256, and 11774413), the Strategic Priority Research Program (B) (Grant No. XDB07030100) of the Chinese Academy of Sciences, and the New Star of Science and Technology Program of Beijing Municipal Science and Technology Commission. We thank the Laboratory of Microfabrication in the Institute of Physics, Chinese Academy of Sciences for experimental support.

References

1 R. Kirchain and L. Kimerling, *Nat. Photonics*, 2007, **1**, 303–305.
2 E. Ozbay, *Science*, 2006, **311**, 189–193.
3 D. K. Gramotnev and S. I. Bozhevolnyi, *Nat. Photonics*, 2010, **4**, 83–91.
4 H. Wei, D. Pan, S. P. Zhang, Z. P. Li, Q. Li, N. Liu, W. H. Wang and H. X. Xu, *Chem. Rev.*, 2018, **118**, 2882–2926.

5 Y. R. Fang, Z. P. Li, Y. Z. Huang, S. P. Zhang, P. Nordlander, N. J. Halas and H. X. Xu, *Nano Lett.*, 2010, **10**, 1950–1954.
6 H. Wei, D. Pan and H. X. Xu, *Nanoscale*, 2015, **7**, 19053–19059.
7 M. Ayata, Y. Fedoryshyn, W. Heni, B. Baeuerle, A. Josten, M. Zahner, U. Koch, Y. Salamin, C. Hoessbacher, C. Haffner, D. L. Elder, L. R. Dalton and J. Leuthold, *Science*, 2017, **358**, 630–632.
8 N. Liu, H. Wei, J. Li, Z. X. Wang, X. R. Tian, A. L. Pan and H. X. Xu, *Sci. Rep.*, 2013, **3**, 1967.
9 Y. L. Wang, T. Li, L. Wang, H. He, L. Li, Q. J. Wang and S. N. Zhu, *Laser Photonics Rev.*, 2014, **8**, L47–L51.
10 D. Pan, H. Wei, Z. L. Jia and H. X. Xu, *Sci. Rep.*, 2014, **4**, 4993.
11 K. C. Y. Huang, M.-K. Seo, T. Sarmiento, Y. Huo, J. S. Harris and M. L. Brongersma, *Nat. Photonics*, 2014, **8**, 244–249.
12 K. M. Goodfellow, C. Chakraborty, R. Beams, L. Novotny and A. N. Vamivakas, *Nano Lett.*, 2015, **15**, 5477–5481.
13 H. Wei, Z. P. Li, X. R. Tian, Z. X. Wang, F. Z. Cong, N. Liu, S. P. Zhang, P. Nordlander, N. J. Halas and H. X. Xu, *Nano Lett.*, 2011, **11**, 471–475.
14 H. Wei, Z. X. Wang, X. R. Tian, M. Kall and H. X. Xu, *Nat. Commun.*, 2011, **2**, 387.
15 Y. L. Fu, X. Y. Hu, C. C. Lu, S. Yue, H. Yang and Q. H. Gong, *Nano Lett.*, 2012, **12**, 5784–5790.
16 S. Viarbitskaya, A. Teulle, R. Marty, J. Sharma, C. Girard, A. Arbouet and E. Dujardin, *Nat. Mater.*, 2013, **12**, 426–432.
17 D. Pan, H. Wei and H. X. Xu, *Opt. Express*, 2013, **21**, 9556–9562.
18 H. Ditlbacher, A. Hohenau, D. Wagner, U. Kreibig, M. Rogers, F. Hofer, F. R. Aussenegg and J. R. Krenn, *Phys. Rev. Lett.*, 2005, **95**, 257403.
19 A. W. Sanders, D. A. Routenberg, B. J. Wiley, Y. N. Xia, E. R. Dufresne and M. A. Reed, *Nano Lett.*, 2006, **6**, 1822–1826.
20 M. W. Knight, N. K. Grady, R. Bardhan, F. Hao, P. Nordlander and N. J. Halas, *Nano Lett.*, 2007, **7**, 2346–2350.
21 S. P. Zhang, H. Wei, K. Bao, U. Hakanson, N. J. Halas, P. Nordlander and H. X. Xu, *Phys. Rev. Lett.*, 2011, **107**, 096801.
22 D. Pan, H. Wei, L. Gao and H. X. Xu, *Phys. Rev. Lett.*, 2016, **117**, 166803.
23 M. Allione, V. V. Temnov, Y. Fedutik, U. Woggon and M. V. Artemyev, *Nano Lett.*, 2008, **8**, 31–35.
24 P. Kusar, C. Gruber, A. Hohenau and J. R. Krenn, *Nano Lett.*, 2012, **12**, 661–665.
25 D. E. Chang, A. S. Sorensen, P. R. Hemmer and M. D. Lukin, *Phys. Rev. Lett.*, 2006, **97**, 053002.
26 A. V. Akimov, A. Mukherjee, C. L. Yu, D. E. Chang, A. S. Zibrov, P. R. Hemmer, H. Park and M. D. Lukin, *Nature*, 2007, **450**, 402–406.
27 H. Wei, D. Ratchford, X. Q. Li, H. X. Xu and C.-K. Shih, *Nano Lett.*, 2009, **9**, 4168–4171.
28 R. Kolesov, B. Grotz, G. Balasubramanian, R. J. Stöhr, A. A. L. Nicolet, P. R. Hemmer, F. Jelezko and J. Wrachtrup, *Nat. Phys.*, 2009, **5**, 470–474.
29 A. Huck, S. Kumar, A. Shakoor and U. L. Andersen, *Phys. Rev. Lett.*, 2011, **106**, 096801.
30 Q. Li, H. Wei and H. X. Xu, *Nano Lett.*, 2014, **14**, 3358–3363.
31 Q. Li, H. Wei and H. X. Xu, *Nano Lett.*, 2015, **15**, 8181–8187.
32 Q. Li, D. Pan, H. Wei and H. X. Xu, *Nano Lett.*, 2018, **18**, 2009–2015.
33 X. Q. Wu, Y. Xiao, C. Meng, X. N. Zhang, S. L. Yu, Y. P. Wang, C. X. Yang, X. Guo, C. Z. Ning and L. M. Tong, *Nano Lett.*, 2013, **13**, 5654–5659.
34 X. Guo, M. Qiu, J. M. Bao, B. J. Wiley, Q. Yang, X. N. Zhang, Y. G. Ma, H. K. Yu and L. M. Tong, *Nano Lett.*, 2009, **9**, 4515–4519.
35 P. Geisler, E. Krauss, G. Razinskas and B. Hecht, *ACS Photonics*, 2017, **4**, 1615–1620.
36 J. S. Huang, V. Callegari, P. Geisler, C. Bruning, J. Kern, J. C. Prangsma, X. Wu, T. Feichtner, J. Ziegler, P. Weinmann, M. Kamp, A. Forchel, P. Biagioni, U. Sennhauser and B. Hecht, *Nat. Commun.*, 2010, **1**, 150.
37 S. Kumar, Y. W. Lu, A. Huck and U. L. Andersen, *Opt. Express*, 2012, **20**, 24614–24622.
38 R. Könenkamp, R. C. Word, J. P. S. Fitzgerald, A. Nadarajah and S. D. Saliba, *Appl. Phys. Lett.*, 2012, **101**, 141114.
39 P. Rai-Choudhury, *Handbook of Microlithography, Micromachining & Microfabrication*, SPIE Press, Washington, DC, 1997.
40 P. B. Johnson and R. W. Christy, *Phys. Rev. B: Condens. Matter Mater. Phys.*, 1972, **6**, 4370–4379.
41 I. H. Malitson and M. J. Dodge, *J. Opt. Soc. Am.*, 1972, **62**, 1405.
42 H. Aouani, J. Wenger, D. Gérard, H. Rigneault, E. Devaux, T. W. Ebbesen, F. Mahdavi, T. Xu and S. Blair, *ACS Nano*, 2009, **3**, 2043–2048.
43 Y. Chen, Z. Li, Q. Xiang, Y. Wang, Z. Zhang and H. Duan, *Nanotechnology*, 2015, **26**, 405301.
44 T. G. Habteyes, S. Dhuey, E. Wood, D. Gargas, S. Cabrini, P. J. Schuck, A. P. Alivisatos and S. R. Leone, *ACS Nano*, 2012, **6**, 5702–5709.
45 J.-C. Tinguely, I. Sow, C. Leiner, J. Grand, A. Hohenau, N. Felidj, J. Aubard and J. R. Krenn, *BioNanoScience*, 2011, **1**, 128–135.
46 F. F. Zhang, J. Proust, D. Gérard, J. Plain and J. Martin, *J. Phys. Chem. C*, 2017, **121**, 7429–7434.
47 R. Zia, M. D. Selker and M. L. Brongersma, *Phys. Rev. B: Condens. Matter Mater. Phys.*, 2005, **71**, 165431.
48 Z. L. Jia, H. Wei, D. Pan and H. X. Xu, *Nanoscale*, 2016, **8**, 20118–20124.